Criticality governs response dynamics and entrainment of periodically forced ghost cycles

Daniel Koch [1,*] Ulrike Feudel [2] and Aneta Koseska [1,†]

[1]*Cellular Computations and Learning, Max Planck Institute for Neurobiology of Behavior - caesar, Ludwig-Erhard-Allee 2, 53175 Bonn, Germany*

[2]*Theoretische Physik/Komplexe Systeme, ICBM, Carl von Ossietzky Universität Oldenburg, Oldenburg, Germany*

(Received 10 February 2025; accepted 10 June 2025; published 8 July 2025)

Many natural and engineered systems display oscillations that are characterized by multiple timescales. Typically, such systems are described as slow-fast systems, where the slow dynamics result from a hyperbolic slow manifold that guides the movement of the system's trajectories. Recently, we have provided an alternative description in which the slow timescale results from Lyapunov-unstable transient dynamics of connected dynamical ghosts that form a closed orbit termed ghost cycle. Here, we investigate the response properties of both types of systems to external forcing. Using the classical Van der Pol oscillator and modified versions of this model that correspond to a one-ghost and a two-ghost cycle, respectively, we find significant differences in the responses of slow-fast systems and ghost cycles, including increased entrainment regions of the latter. Nonautonomous model analysis reveals that the differences stem from a continuous remodeling of the attractor landscape of the ghost cycle models, enabled by being organized close to saddle-node on invariant cycle bifurcations, in contrast to a qualitatively unaltered attractor landscape of the slow-fast system. We further demonstrate that the observed features occur in various systems with ghost cycles regardless of the exact mathematical model formulation leading to those ghost cycles, making them likely to apply to many other models with ghost cycles across different disciplines and contexts. We thus propose that systems containing ghost cycles display increased flexibility and responsiveness to continuous environmental changes.

DOI: 10.1103/3d9z-qrb1

I. INTRODUCTION

Periodic or oscillatory behavior is characteristic for a range of natural or engineered systems, including respiration and circadian clocks [1], pulsatile hormone secretion [2], neural and cardiac rhythms [3,4], chemical and biochemical reactions [5,6], population cycles of predator-prey types [7–9], insect outbreaks [10], climate phenomena [11–14], and lasers [15], to name but a few. One of the most common type of periodic behaviors are relaxation oscillations, characterized by repeated switching between slow and fast motions. These processes are generally modeled by singularly perturbed ordinary differential equations [16,17] of the form

$$\varepsilon\dot{x} = f(x, y, \lambda, \varepsilon), \quad \dot{y} = g(x, y, \lambda, \varepsilon), \tag{1}$$

where $(x, y) \in \mathbb{R}^n \times \mathbb{R}^m$, λ are the system's parameter, and $0 < \varepsilon \ll 1$ is a special parameter that determines the timescale separation. In the singular limit $\varepsilon = 0$, Eq. (1) is called the *reduced system*, which can be used to understand the slow flow of the original system. Conversely, setting $\varepsilon = 0$ after rescaling Eq. (1) by $\tau = \frac{t}{\varepsilon}$ yields the *layered system* in fast time. The *critical manifold* $C_0 = \{(x, y) \in \mathbb{R}^n \times \mathbb{R}^m | f(x, y, \lambda, 0) = 0\}$ determines whether the reduced or the layered system is the appropriate approximation of the system's dynamics: Close enough to C_0, we expect the dynamics to align with the slow flow on the critical manifold, whereas phase space regions farther away from C_0 will obey the layered system [16]. Fenichel's theorem guarantees that for small enough $\varepsilon > 0$, provided smoothness and hyperbolicity conditions are met, the critical manifold perturbs to an invariant *slow manifold* S that retains the hyperbolicity of the original critical manifold and still allows the dynamics to be approximated by the reduced system [16,18,19]. Fenichel's results thereby provide the mathematical foundation for understanding slow-fast dynamics, ensuring that the slow manifold faithfully captures the system's long-term behavior near the critical manifold.

There is a growing recognition, however, that a multitude of naturally occurring processes are characterized by sequences of quasistable regimes in which each regime appears stable for a limited, but potentially very long, period, before rapidly transitioning to another quasistable regime. This includes, for example, neuronal activity dynamics [20], e.g., during rest and behavioral or sensory tasks [21–23], embryonic development [24,25], long transients of species compositions in coral reefs [26], and other ecological systems [27]. Such dynamics cannot always be fully captured by the asymptotic description of slow-fast systems. Thus, complementary to the idea of attractors governing the system's dynamics, it has been proposed that long transients can emerge due to the system's dynamics lingering near a saddle fixed point or by being guided through heteroclinic

*Contact author: dkoch.research@protonmail.com
†Contact author: aneta.koseska@mpinb.mpg.de

Published by the American Physical Society under the terms of the Creative Commons Attribution 4.0 International license. Further distribution of this work must maintain attribution to the author(s) and the published article's title, journal citation, and DOI. Open access publication funded by Max Planck Society.

channels and cycles [28–30]. Complementing this description, we recently proposed that sequential quasistable dynamics can emerge via sequential and cyclical organization of ghost attractors in phase space [31], termed *ghost channels* and *ghost cycles*, respectively. The emergence of ghost cycles is dynamically equivalent to an organization in the vicinity of one or multiple co-occurring saddle-node on invariant cycle (SNIC) bifurcations. In this case, the dynamics of the system is organized around a set that is nonhyperbolic in the sense that it features a spatial distribution of the largest eigenvalues ranging from negative to positive while passing through zero [31]. This so-called *ghost-attracting set* guides the flow in phase space and transiently traps trajectories, but is not stable in the sense of Lyapunov [31–33]. Thus, experimental observations of processes that have quasistable dynamics with fast switching between them can emerge from different dynamical mechanisms in autonomous systems that are often indistinguishable when considering solely their time series characteristics.

However, natural systems do not operate in isolation but are rather subjected to external influences that vary over space and time. This is true for biological cells, where the signals are produced by the neighboring cells or tissues, neuronal systems that are continuously exposed to non-stationary sensory signals, as it is for ecological systems that are influenced by the weather, climate, seasonal changes, or human-induced forces. The type of autonomous dynamics and the mechanism through which it arises play a major role in how the system responds to such external forcing. To investigate whether attractor-governed slow-fast systems and ghost cycles characterized by nonasymptotic transient dynamics differ in their response to external forcing, we study here the entrainment and response characteristics of the Van der Pol oscillator (VdP) as a prototypical slow-fast system, and two modified Van der Pol systems which exhibit one-ghost (VdP_{1g}) and two-ghost (VdP_{2g}) cycles, respectively. We show that under low amplitude periodic forcing, ghost cycles display increased entrainability compared to slow-fast systems, i.e., the 1:1 entrainment dominates the behavior. Quantifying the local phase-space dynamics, we demonstrate that the difference arises from qualitative disparate mechanisms guiding the response dynamics: continuous nonautonomously driven remodeling of the attractor landscape, enabled by the critical organization of the ghost cycle vs. manifold-governed dynamics for the slow-fast system. We show that the observed entrainment features of the ghost cycles occur in various models from different disciplines and propose that multi-scale dynamics emerging from long transients, in contrast to slow-fast systems, likely provide broader adaptation to external signals.

II. RESULTS

A. Introducing ghosts in the Van der Pol system: Effect on the system's timescales

Let us consider the VdP model [34], a classical slow-fast system given by the equations [16]

$$\begin{aligned}\dot{x} &= \frac{1}{\varepsilon}\left(x - \frac{x^3}{3} + y\right)\\ \dot{y} &= -x + A\ \sin(\omega t),\end{aligned} \tag{2}$$

where ε is the timescale separation parameter, and A and ω are the amplitude and the frequency of external periodic forcing, respectively. In the autonomous case ($A = 0$) and for ε sufficiently small (here $\varepsilon = \frac{1}{50}$), the VdP oscillator exhibits a pronounced separation of the slow and fast timescales and oscillates with an intrinsic frequency ω_0. The critical manifold of this system is the cubic curve $y = x^3/3 - x$, which is also the x-nullcline of the system, whereas the y-nullcline is defined by the line $x = 0$ [Fig. 1(a), left]. The manifold is normally hyperbolic away from the local maximum (p_-) and minimum (p_+) of the cubic, and these fold points decompose it into two slow and attracting ($C_0^{a,+}$, $C_0^{a,-}$), and one repelling branch (C_0^r). Thus, a trajectory starting on the critical manifold moves along the slow branch before rapidly switching to the second slow branch at the fold points p_+ and p_-. This leads to time series [Fig. 1(c), left] characterized by two distinct trajectory velocities indicative of a slow-fast system, which is further reflected in the bimodal velocity distribution [Fig. 1(d), left].

Ghost cycles, on the other hand, do not rely on the existence of an invariant hyperbolic manifold. In fact, ghost attracting sets are characterized by an eigenvalue distribution from negative to positive, including zero eigenvalues, resulting in the establishment of a slow timescale in the system [31]. Generally, ghost attractors emerge when a system is close to a saddle-node bifurcation (e.g., SNIC), and in planar systems when the nullclines of the system are close to each other but do not intersect. Thus, by manipulating the shape of the y-nullcline, it is possible to introduce ghost dynamics in the VdP system, in addition to the slow-fast dynamics. As a simple way to achieve this, we devised modifications of the VdP system that geometrically alter the shape of the y-nullcline, such that it bends toward the x-nullcline in one or more areas of the phase space. Consider the following modifications:

(VdP_{1g} system)

$$\begin{aligned}\dot{x} &= \frac{1}{\varepsilon}\left(x - \frac{x^3}{3} + y\right)\\ \dot{y} &= -x + \alpha\left(y + 0.7 - \frac{(y+0.7)^3}{3}\right)\\ &\quad\times\left(\frac{1+\tanh(y+0.7)}{2}\right)^{10} + A\ \sin(\omega t),\end{aligned} \tag{3}$$

and

(VdP_{2g} system)

$$\begin{aligned}\dot{x} &= \frac{1}{\varepsilon}\left(x - \frac{x^3}{3} + y\right)\\ \dot{y} &= -x + \alpha\left(y - \frac{y^3}{3}\right) + A\ \sin(\omega t).\end{aligned} \tag{4}$$

For $\alpha = 0$, both systems, Eqs. (3) and (4) are equivalent to the classical Van der Pol oscillator [Eqs. (2)]. Setting $\alpha > 0$, however, controls the shape of the y-nullcline such that it bends and approaches the vicinity of the x-nullcline once (VdP_{1g}) or twice (VdP_{2g}), giving rise to a single or to two ghosts [Fig. 1(a), right panel]. Formally, this corresponds to a parametric organization before single or multiple SNIC bifurcations that destroy the limit cycle at a critical value α_{crit}

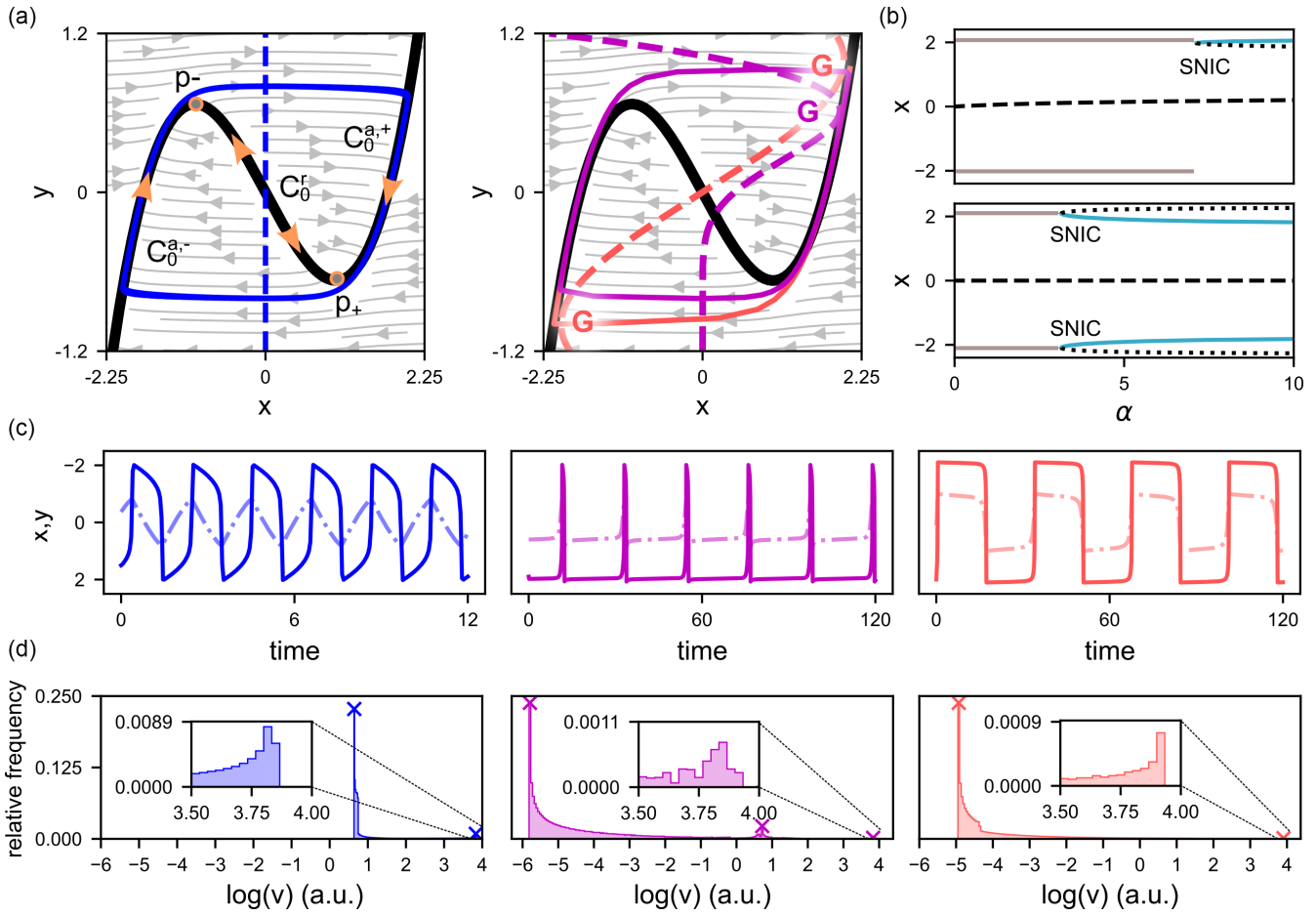


FIG. 1. Emergence of ghost cycles in a modified VdP oscillator. (a), left panel: phase space organization of the original VdP model. Black line: x-nullcline, dashed blue line: y-nullcline, continuous blue line: system's trajectory. The critical manifold of the VdP corresponds to the x-nullcline and consists of three branches $C_0^{a,+}, C_0^r, C_0^{a,-}$, the slow flow along which is indicated by orange arrowheads. Right panel: the y-nullclines of VdP_{1g} (purple dashed line) and VdP_{2g} (red dashed line) models for $\alpha = 7.121$ and $\alpha = 3.135$, respectively, demonstrating emergence of ghost attractors (G). Trajectories are shown in continuous purple (VdP_{1g}) and red (VdP_{2g}) lines. (b) Bifurcation analysis of the VdP_{1g} (top) and VdP_{2g} (bottom). Dashed black line: unstable focus; gray line: stable limit cycle; dotted black line: saddle; teal line: stable fixed point. SNIC bifurcations at $\alpha = 7.131$ and $\alpha = 3.145$, respectively. (c) Simulated time series of x- (continuous line) and y-variables (dashed/dotted line) of the VdP (left), VdP_{1g} (middle), and VdP_{2g} (right) systems. (d) Histograms of the velocity distributions along the systems' trajectories. Indicated peaks are taken as representative timescales of the systems.

[Fig. 1(b)]. The rationale behind both VdP_{1g} and VdP_{2g} is to introduce a similar cubic term for $\dot{y}$ as for $\dot{x}$ that leads to the bending of the nullcline and to scale it by α to induce the SNIC bifurcations as the nullclines intersect for high enough α. The factor $((1 + \tanh(y + 0.7))/2)^{10}$ in Eq. (3) ensures that the y-nullcline bends only in the upper part of the phase space of VdP_{1g}, leading merely to a single SNIC bifurcation as α increases. The only geometrical constraint for the SNICs to occur is that the nullclines approach each other on the periodic orbit and not outside of it—which is the reason for the additional y-offset of 0.7 in Eq. (3). Note, however, that the particular functional forms introduced to generate VdP_{1g} and VdP_{2g} are not unique and other functions that achieve comparable geometric effects can be chosen.

Introducing a single ghost in the VdP dynamics effectively does not change the shape of the oscillation's peaks. However, longer transients between the peaks are present, resulting from the system's dynamics visiting the ghost that is formed [Fig. 1(c), middle]. This additional slow timescale that arises from trapping in the ghost is also visible as an additional peak in the distribution of the velocity quantified from the system's trajectories [Fig. 1(d), middle]. In the VdP_{2g} system, however, a two-ghost cycle emerges that now determines the system's dynamics: while rapid transitions along the x-direction still occur, the time during which the trajectory is trapped in the ghost regions fully dominates the slow dynamics [Fig. 1(c), right]. Comparing the dynamics of the fast variable of VdP and VdP_{2g} systems on the critical manifolds shows that the ghost-induced slow timescale indeed dominates the slow dynamics of the VdP_{2g} system, such that the dynamics on the critical manifold plays only a negligible role in the system's dynamics (Supplemental Material Fig. 1) [35]. This is also visible in the velocity distribution of the VdP_{2g} system, which reveals only the peaks of the fast timescale and the ghost-induced slow timescale [Fig. 1(d), right]. Thus, the slow timescale in the VdP and the VdP_{2g} systems are governed by different dynamical mechanisms. Given that the period of the VdP system is shorter than that of the ghost cycles

(VdP_{2g}), we scale the VdP equations [Eqs. (2)] by a factor $\tau = 16.5$ ($\tau\dot{x}, \tau\dot{y}$), such that both periods are approximately equal (Supplemental Material Fig. 2), ensuring thereby that differences in the subsequent analyses are due to qualitative features of these systems, reflecting the different dynamical mechanisms, and not merely the differences in the periods or effective timescales.

B. Response to periodic forcing

To investigate whether the different mechanisms through which the slow timescales emerge in these systems influence how they respond to time-varying signals, we subject the VdP, VdP_{1g}, and VdP_{2g} systems to periodic forcing, and numerically explore their behavior. To begin with, we study the entrainment of these systems to the forcing signal by quantifying the corresponding Arnold tongues [36]. Arnold tongues visualize the entrainment behavior of forced oscillatory systems and represent areas in the forcing amplitude-frequency space in which the system is mode-locked or phase-locked to the external forcing, as represented by a constant winding or rotation number ρ. Typically, major entrainment areas where the forced oscillator exhibits n periods for m periods of external forcing ($n : m$ entrainment) are highlighted. We focus here on low amplitude forcing ($0 < A \leqslant 0.25$), and for each system, we scan an interval of forcing frequencies ranging from 0.1- to 10-fold of the intrinsic frequency (ω_0) of the autonomous system.

The scaled VdP system exhibits a typical response to periodic forcing, where 1:1 entrainment is most prominent, and other $n : m \neq 1 : 1$ entrainment regions exist in narrow parameter ranges [Fig. 2(a), left]. The single ghost introduced in VdP_{1g}, in contrast, notably changes the response properties of the system: the Arnold tongues are much wider already at low amplitudes of the external forcing compared to the classical VdP oscillator, and their width is only marginally affected as the amplitude increases [Fig. 2(a), middle]. For the VdP_{2g} system, however, the difference in the system's responsiveness is even more pronounced: the majority of the two-parameter plane spanned by the amplitude and frequency of the forcing is filled by a large 1:1-entrainment tongue [Fig. 2(a), right], despite having the same intrinsic period as the scaled VdP system.

We next examine how robust the observed entrainment properties are in the presence of noise which we modeled as Gaussian white noise that is introduced as an additive term at each time step, yielding a stochastic differential equation in Ito form, $X(t) = f(X(t), t)dt + \sigma dW(t)$, where dt denotes the step size, $\sigma(t)$ describes the additive noise level, and $W(t)$ denotes a Wiener process whose independent increments follow a normal distribution with ($\mu = 0, SD = 1$) and amplitude $\sqrt{\Delta t}$. Since Arnold tongues are not defined in the presence of noise, one can instead plot the difference between the observed frequency and the forcing frequency as a function of the forcing frequency at a given amplitude [36]. Plateaus in these plots essentially correspond to cross sections through the Arnold tongues. Focusing on the 1:1 entrainment of the three systems at an amplitude of $A = 0.125$ [cf. dashed red lines in Fig. 2(a)], we find that the plateaus corresponding to the 1:1-tongues at $\sigma = 10^{-5}$ remain almost identical to the noise-free case, whereas for noise levels at which high variability in the period is observed ($\sigma = 2 \times 10^{-2}$), the plateaus corresponding to the 1 : 1-tongues are slightly narrower and characterized by larger errors [Fig. 2(b)]. Thus, the functional response mostly reflects the characteristics of the noise-free case, suggesting that the observed entrainment properties are robust in the presence of noise.

Quantifying the interspike-interval (ISI) distribution as a function of the forcing frequency at a fixed amplitude ($A = 0.125$) reveals further differences in the response dynamics between the three systems. In the case of the scaled VdP system, the ISI distributions outside the entrainment bands are broad and dispersed [Fig. 2(c), left], although the overall ISI distribution remains narrow and close to the intrinsic ISI in the absence of forcing. The ISI distribution of the VdP_{1g} system, on the other hand, is bimodal at low forcing frequencies, and transits to a unimodal one above $\omega \approx 1.6 \cdot \omega_0$ [Fig. 2(c), middle]. This bimodal ISI distribution results from the emergence of bursting dynamics with trains of rapid spiking followed by quiescent phases in between (Supplemental Material Fig. 3). In the case of the VdP_{2g} system, a unimodal distribution with decreasing ISI duration for increasing forcing frequency is observed, consistent with the large Arnold tongue for the 1:1 entrainment regime [Fig. 2(c), right]. At higher driving frequencies, on the other hand, as the ISI duration begins to decrease again, time courses reveal a quick divergence of the trajectories for small perturbations of the initial conditions [Fig. 2(d)], indicative of chaotic dynamics. Time-course simulations, Poincaré-sections, and calculation of the largest Lyapunov exponents show that only the VdP_{2g} system exhibits chaotic behavior in the (A, ω)-space considered here, which is not the case for the VdP and VdP_{1g} systems [Fig. 2(e), cyan crosses in Fig. 2(a), and Supplemental Material Fig. 3].

We next study the origin of the different response properties of the VdP oscillator and its ghost cycle variants in more detail by considering the periodically forced models as nonautonomous systems. Generally, in nonautonomous systems, the geometry (positioning, shape, and size of the attractors) or topology (number or stability of the attractors) of the underlying phase space can change over time [37–39]. To quantify these changes as a function of the periodic forcing, we analyze the phase-space configuration of the three different systems at different time points via snapshots taken at defined stages of the forcing (as done in Ref. [40]).

Applying this approach to the VdP system, we find that periodic forcing leads to a slight shift of the y-nullcline back and forth along the x-axis which changes the position of the system's unstable focus, but without inducing qualitative changes in the topology of the attractor landscape [Figs. 3(a1)–3(a3), Supplemental Material Video 1]. Thus, the response of the forced oscillator is solely governed by the slow-fast dynamics of the autonomous systems, explaining the typical entrainment response and time courses.

In the VdP_{1g} system, in contrast, external forcing continuously remodels the attractor landscape. New fixed points (stable and saddle) emerge via a SNIC bifurcation such that the stable fixed point traps the system trajectory [Fig. 3(b1)], while at a later time, the fixed points and ghost attractor are destroyed by moving the x- and the y-nullclines farther apart

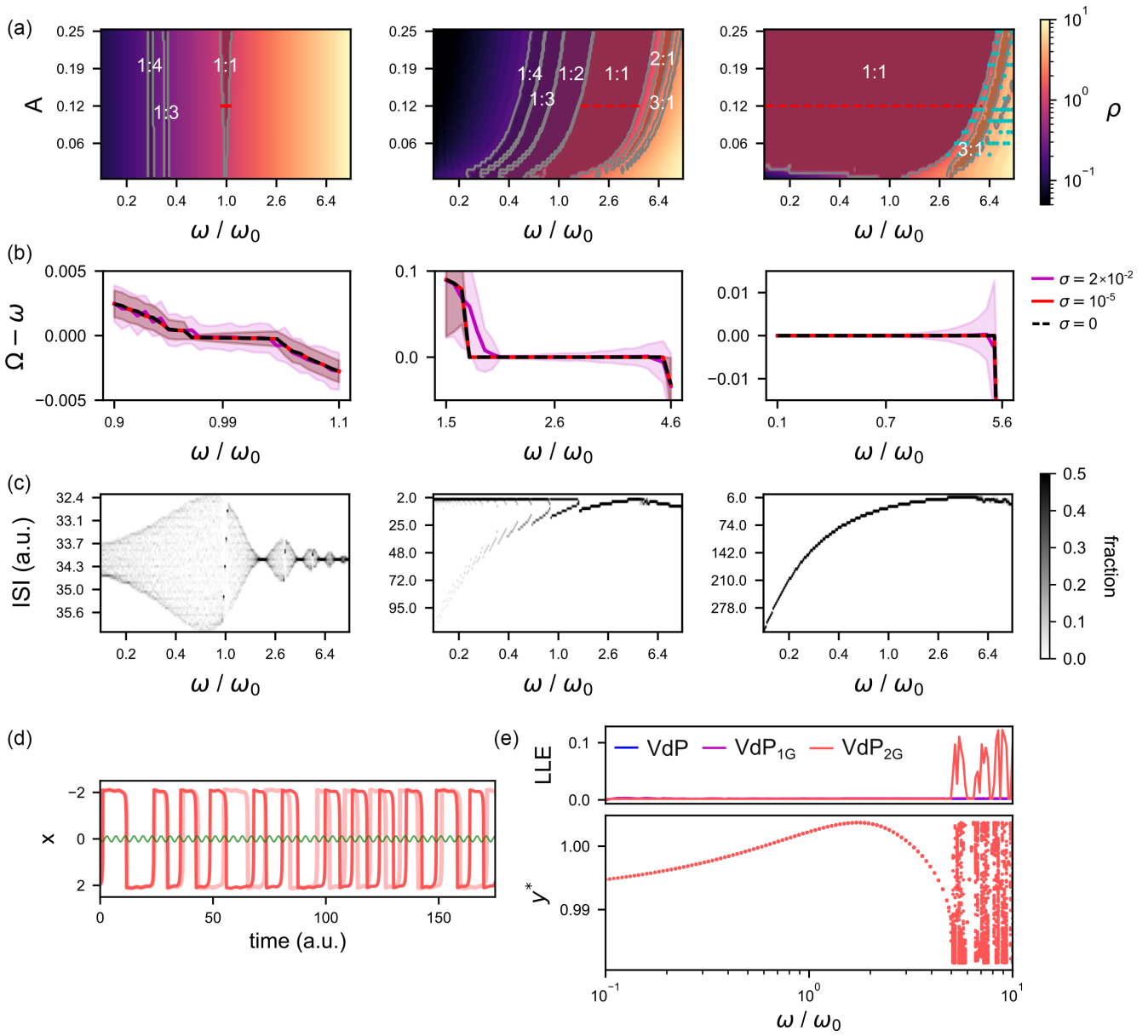


FIG. 2. Response to periodic forcing. (a) Arnold tongues indicating areas of n:m entrainment for the VdP (left), VdP_{1g} (middle), and VdP_{2g} (right) systems as a function of the amplitude A and frequency (ω; normalized to the frequency of the unforced system, ω_0) of the forcing. Only tongues making up at least 1% of the parameter space are shown. Color encodes the winding number $\rho = \frac{T_{\mathrm{out}}}{T_{\mathrm{in}}}$; teal crosses indicate largest Lyapunov exponents >0. (b) Difference of the observed frequency Ω and the driving frequency ω at various noise intensities in the parameter range indicated by the dashed red lines in (a). Plateaus correspond to cross sections through the 1:1 entrainment tongues. (c) Distribution of the interspike intervals (ISIs) as a function of the forcing frequency for the VdP (left), VdP_{1g} (middle), and VdP_{2g} (right) system. (d) Exemplary time series for different initial conditions of the VdP_{2g} system at high forcing frequencies ($A = 0.1$, $\omega = 10 \cdot \omega_0$). (e) Top: Largest Lyapunov exponents (LLE) as a function of the forcing frequency. Bottom: Orbit diagram based on Poincaré-sections of the VdP_{2g} system.

again [Figs. 3(b2) and 3(b3)]. This creates a gating mechanism in which the trajectory quickly cycles along the orbit of the VdP_{1g} system when the ghost attractor is absent but is transiently captured by the emergence of the stable fixed point at sufficient forcing strength, which in turn explains the widening of the Arnold tongues (Supplemental Material Video 2). If the forcing frequency is sufficiently low, the remodeling of the attractor landscape proceeds slowly enough so that multiple cycles on the periodic orbit can be completed before the trajectory is recaptured by the emergence of the stable fixed point again, explaining why the system exhibits bursting dynamics (Supplemental Material Video 3). This mechanism is equivalent to the previously described parabolic circle/circle bursting [4], except that the role of the slow variable driving the system back and forth the SNICs is played by the periodic forcing signal.

Similarly, in the VdP_{2g} system, the periodic forcing results in a continuous alternation between the creation and destruction of stable fixed points in opposite areas of the phase space [Figs. 3(c1)–3(c3)]: when the input moves the y-nullcline to

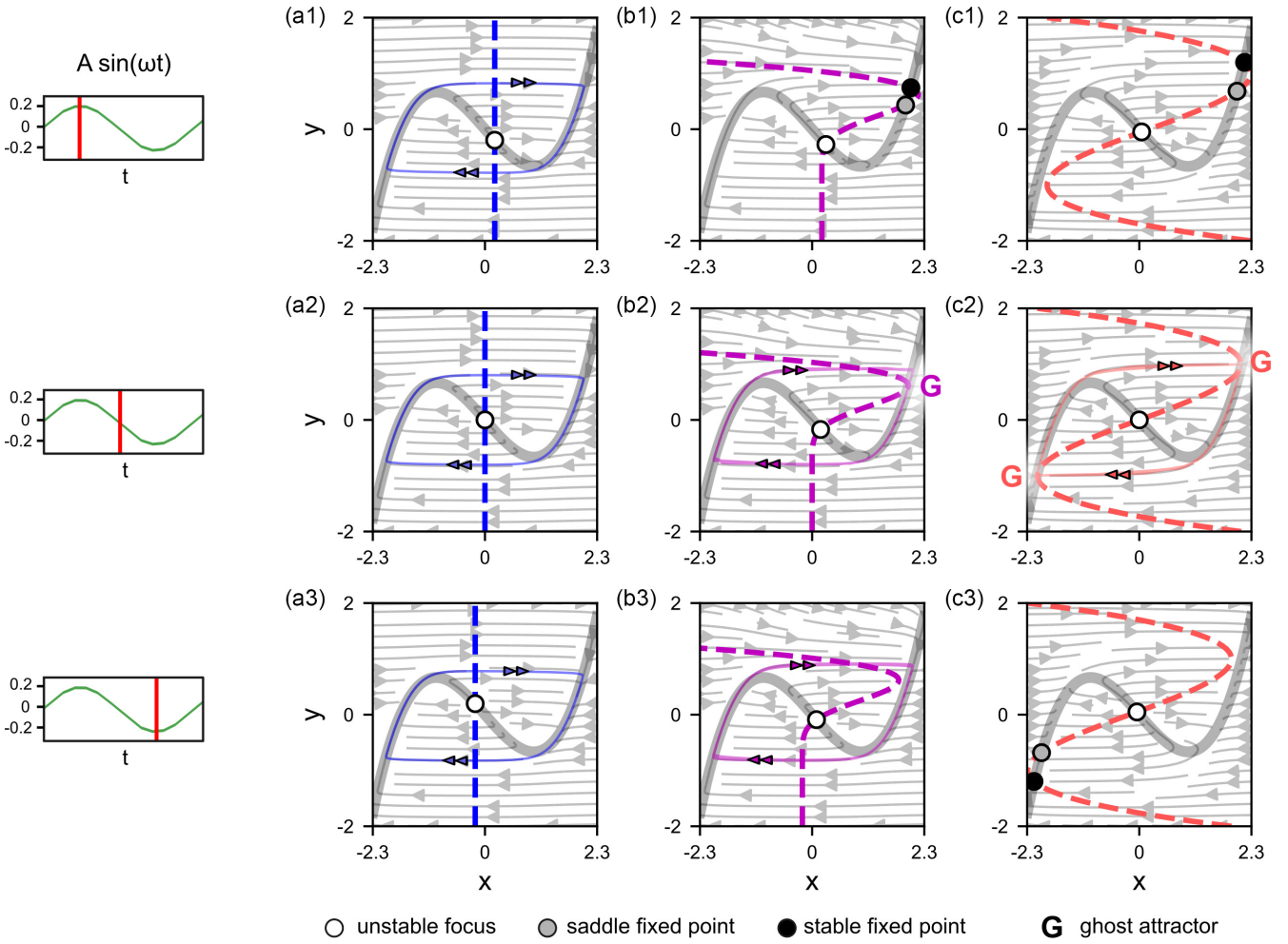


FIG. 3. Phase-plane analysis at different stages of forcing. (a1)–(a3) In the original VdP system, low amplitude external forcing leads to shifting of the y-nullcline back and forth along the x-axis, without inducing major qualitative changes in the attractor landscape. (b1)–(b3) In the VdP_{1g} system, shifting of the y-nullcline back and forth along the x-axis leads to a periodic disappearance of the ghost attractor either by creation of a new fixed point via a SNIC bifurcation (b1) such that the trajectory is trapped here, or via moving the nullclines farther apart (b3), thereby losing the slow timescale from the ghost. (c1)–(c3) In the VdP_{2g} system, the external forcing leads to alternate creation and destruction of fixed points via two opposite SNIC bifurcations, and thereby periodic disappearance of the ghost attractors. Double arrowheads denote fast transitions of the trajectory. Snapshots at $A\sin(\omega t) = 0.2$ (top row), $A\sin(\omega t) = 0$ (middle row), and $A\sin(\omega t) = -0.2$ (bottom row).

the right, a stable and a saddle fixed point are created in the upper right area via a SNIC bifurcation, while in the lower left area of the phase space, a stable and a saddle fixed point are being destroyed. Conversely, moving the y-nullcline toward the left results in the equivalent situation in the opposite phase-space area in the lower left. This leads to a situation in which the trajectory, whenever it is released from one corner of the phase space after the destruction of the stable fixed point, is immediately captured by the stable fixed point that is generated at the other side (Supplemental Material Video 4). Thus, the trajectory can only move along half of the orbit at once, explaining the ultra-large range of 1:1 entrainment of the VdP_{2g} system. Together, these findings suggest that forcing-induced remodeling of the phase space for the ghost cycles due to their organization at criticality (being close to one or more SNIC bifurcations) is a major factor in the observed response characteristics that significantly differ from those of the standard VdP model as governed by its critical manifold.

Phase-space reorganization is also a major factor in rate-dependent processes (e.g., rate tipping), which are typical for nonautonomous systems [39–42]. To explore if we can understand the entrainment of the VdP_{2g} model as a rate-dependent process, we analyze, using geometric singular perturbation methods, how the presence of the ghost affects the slow dynamics on the critical manifold in response to periodic forcing (cf. Supplemental Material for details). While the critical manifold for both the VdP and VdP_{2g} system is the same ($y = \frac{x^3}{3} - x$), the dynamics on this manifold strongly differ between the two systems, as already described (cf. Supplemental Material Fig. 1). In the autonomous case, these differences stem from a plateau in the potential of the VdP_{2g} system which corresponds to the system's ghost attractor (Supplemental Material Fig. 4). This perspective also allows us to track the potential changes in the nonautonomous case. Before considering the rate at which the potential changes, note that there are two principal ways in which periodic

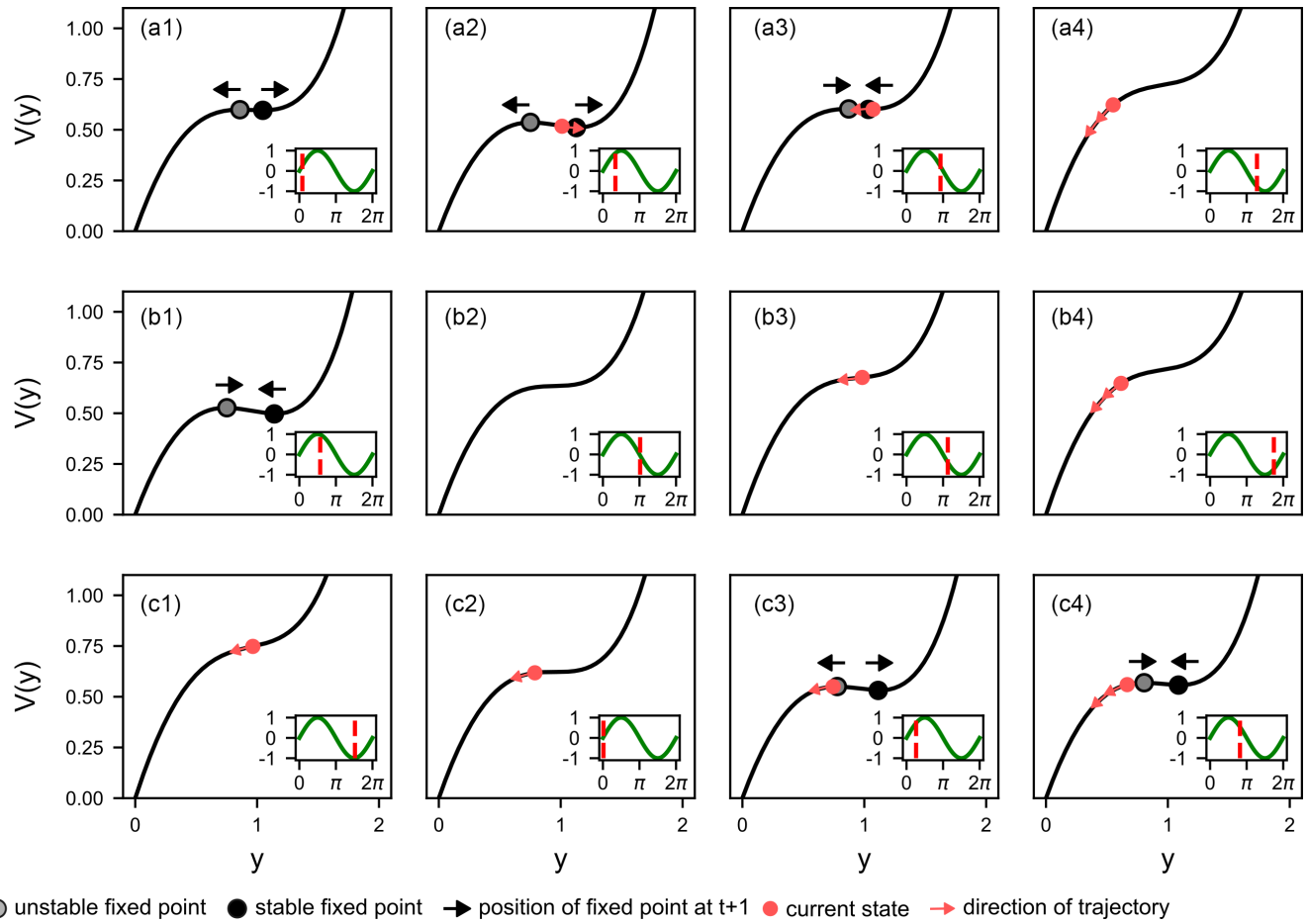


FIG. 4. Loss of entrainment via rate-dependent boundary-crossing in the VdP_{2g} system. Temporal relationship between remodeling of the quasipotential landscape on the critical manifold via SNIC bifurcations and the approach of the trajectory toward the critical manifold for three representative forcing frequencies ((a1)–(a4), $\omega = \omega_0$, within the 1:1-tongue; (b1)–(b4), $\omega = 4.75 \cdot \omega_0$, boundary of the 1:1-tongue; (c1)–(c4), $\omega = 5.25 \cdot \omega_0$, outside of the 1:1-tongue). Forcing amplitude $A = 0.125$ for all three scenarios.

forcing can qualitatively change the potential landscape of the VdP_{2g} system that correspond to different phases of the forcing: First, the forcing can make the plateau steeper, thereby reducing the trapping time at the ghost. Second, if the sign of the forcing is reversed, the plateau becomes more indented, leading to the emergence of local extrema in the potential landscape, which is equivalent to fixed points being created by the SNIC bifurcations. On the other hand, when $A \sin(\omega t) \approx 0$, the plateau persists, allowing the system to be transiently stabilized in the ghost.

To better understand the entrainment of ghost cycles, we next analyze how the rate at which the potential landscape is changing affects the evolution of the VdP_{2g} system's trajectory on this landscape (Fig. 4 and Supplemental Material Videos 5–7). At $\omega = \omega_0$, i.e., well within the 1:1-tongue, the SNIC bifurcation results in the creation of a stable and an unstable fixed point, which sets the shape of the potential [Fig. 4(a1)]. The system's trajectory lags behind this change, reaching the critical manifold on the right side of the unstable fixed point, then moving downhill toward the stable fixed point [Fig. 4(a2)] and following it until the fixed points collide and are destroyed in a reverse SNIC bifurcation [Fig. 4(a3)]. The potential continues to steepen, allowing the trajectory to escape the plateau [Fig. 4(a4)], before the same sequence of events is repeated. See also Supplemental Material Video 5. At the edge of the 1:1-tongue ($\omega = 4.75 \cdot \omega_0$), the qualitative picture slightly differs. First, a reverse SNIC bifurcation destroys the stable and unstable fixed points [Fig. 4(b1)]. Next, the system's trajectory arrives on the critical manifold while the potential still has a pronounced plateau [Figs. 4(b2) and 4(b3)], i.e., the trajectory is trapped at the ghost for a transient period of time, but eventually escapes the critical manifold as the forcing continues to steepen the potential [Fig. 4(b4) and Supplemental Material Video 6]. For $\omega = 5.25 \cdot \omega_0$, outside of the 1:1 tongue, the relationship between potential changes and the arrival of the trajectory on the potential varies from cycle to cycle, with the trajectory typically arriving during the flattening of the potential, before the next creation of fixed points via the SNIC bifurcations takes place [Figs. 4(c1) and 4(c2)]. As the trajectory in this case is positioned left of the unstable fixed point, it does not get trapped at the stable fixed point but is instead pushed away [Figs. 4(c3) and 4(c4) and Supplemental Material Video 7]. As the trajectory's fate depends on which side of the unstable fixed point it is positioned, which in turn depends on the rate at which the potential landscape changes, the loss of entrainment can, therefore, be characterized as a rate-dependent boundary-crossing process [40]. Together, these results demonstrate that the response

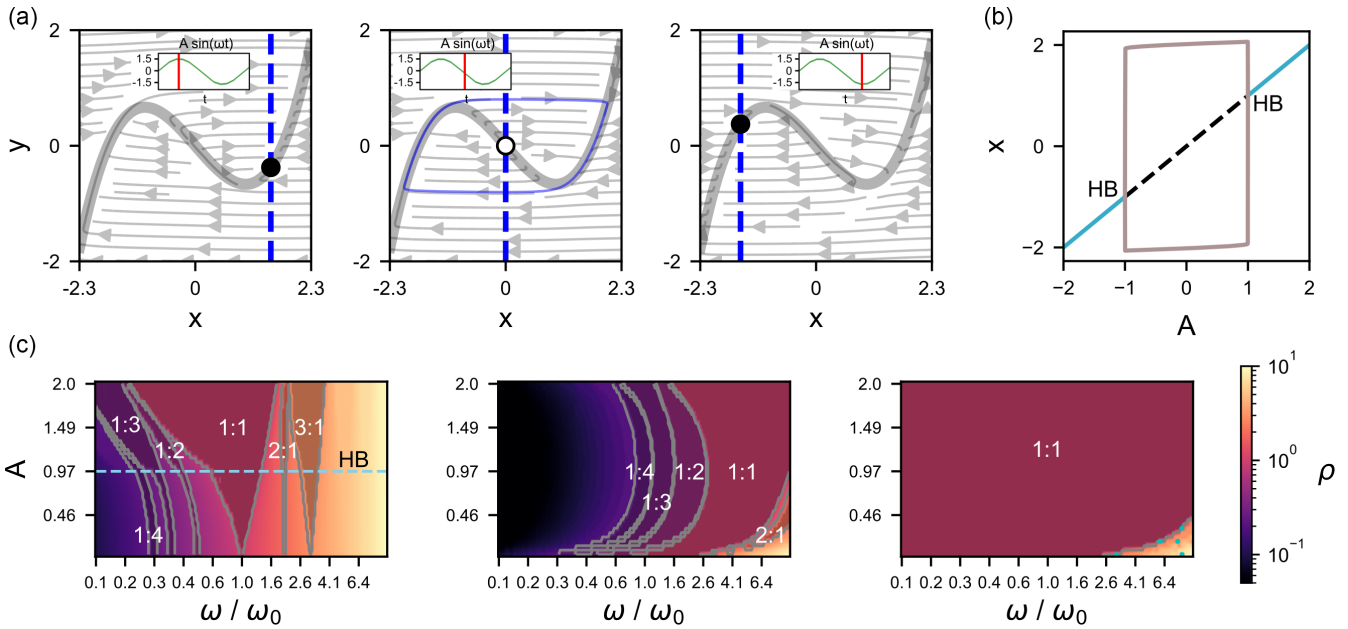


FIG. 5. Response to high-amplitude forcing. (a) Snapshots of the forced VdP system at different timepoints for $A = 1.5$. Black dot: stable fixed point, white dot: unstable focus. (b) Bifurcation diagram of the VdP system with constant forcing using the forcing amplitude A as parameter, showing a Hopf-Bifurcation (HB) at $A = \pm 1$. (c) Arnold-tongue diagrams for forcing amplitudes up to $A = 2$, for VdP, VdP_{1g}, and VdP_{2g} systems (left to right).

properties of ghost cycles are markedly different from the dynamics of classical slow-fast systems in the low amplitude forcing regimes considered here.

To complete the picture, we further consider the response dynamics of the three systems to higher amplitude forcing. Phase plane analysis of the VdP system shows that when the forcing amplitude A is large enough for the y-nullcline of the VdP system to pass the fold points of the x-nullcline, the unstable focus changes its stability and becomes a stable fixed point [Fig. 5(a)]. Using a VdP system with constant forcing for bifurcation analysis to understand the nature of this transition revealed that it corresponds to passing through Hopf-bifurcations (HB) [Fig. 5(b)], and not SNIC-bifurcations as in the VdP_{1g} and VdP_{2g} systems. For forcing amplitudes large enough to pass these HBs, the 1:1 Arnold tongue shows a sudden enlargement [Fig. 5(c), left], but is, however, still significantly narrower compared to the VdP_{2g} system in the same amplitude range [Fig. 5(c), right]. These differences result again from the different mechanisms through which the entrainment arises: while in the VdP_{1g} and VdP_{2g} systems the trajectory closely follows the intersection of the nullclines during entrainment even at fast forcing frequencies, the trajectory of the VdP system continuously lags behind the intersections of the nullclines after passing the HB, mostly being transiently slowed down on the critical manifold and only being trapped by the stable focus fixed point at very low forcing frequencies (Supplemental Material Video 8). Hence, the response dynamics of the VdP system and its ghost variants are governed by different dynamical mechanisms, also at higher forcing amplitudes.

C. Ghost cycles in other models

To demonstrate that the observed response properties of ghost cycles and slow-fast systems described here are guided by different mechanisms and are not peculiarities of the constructed models here, we validate the results using well-established models from other fields. Different parameter regimes of a neuronal and an ecological model are used to study their slow-fast, one-ghost cycle, and two-ghost cycle dynamics, respectively.

1. Slow-fast and one-ghost cycle dynamics in the Morris-Lecar model

To validate the observed dynamics of the one-ghost cycle from the VdP_{1g} system, we consider the Morris-Lecar (ML) model [43] for neuronal dynamics, another typical slow-fast system that features both excitable and oscillatory dynamics. The ML system [44] is given by

$$\begin{aligned} C_m\dot{V} &= -g_L(V - V_L) - g_{Ca}M_\infty(V - V_{Ca}) - g_K N(V - V_K) \\ &\quad + (I_{\mathrm{ext}} + A\ \sin(\omega t)) \\ \dot{N} &= \frac{N_\infty - N}{\tau_N}, \end{aligned} \tag{5}$$

where V is the membrane potential in mV, N is the dimensionless activation variable, and

$$\begin{aligned} M_\infty &= \frac{1}{2}\left(1 + \tanh\left(\frac{V - V_1}{V_2}\right)\right) \\ N_\infty &= \frac{1}{2}\left(1 + \tanh\left(\frac{V - V_3}{V_4}\right)\right) \\ \tau_N &= 1/\left(\phi \cosh\left(\frac{V - V_3}{2V_4}\right)\right). \end{aligned}$$

As before, A is the amplitude and ω the frequency of external periodic forcing. The ML system is parameterized to

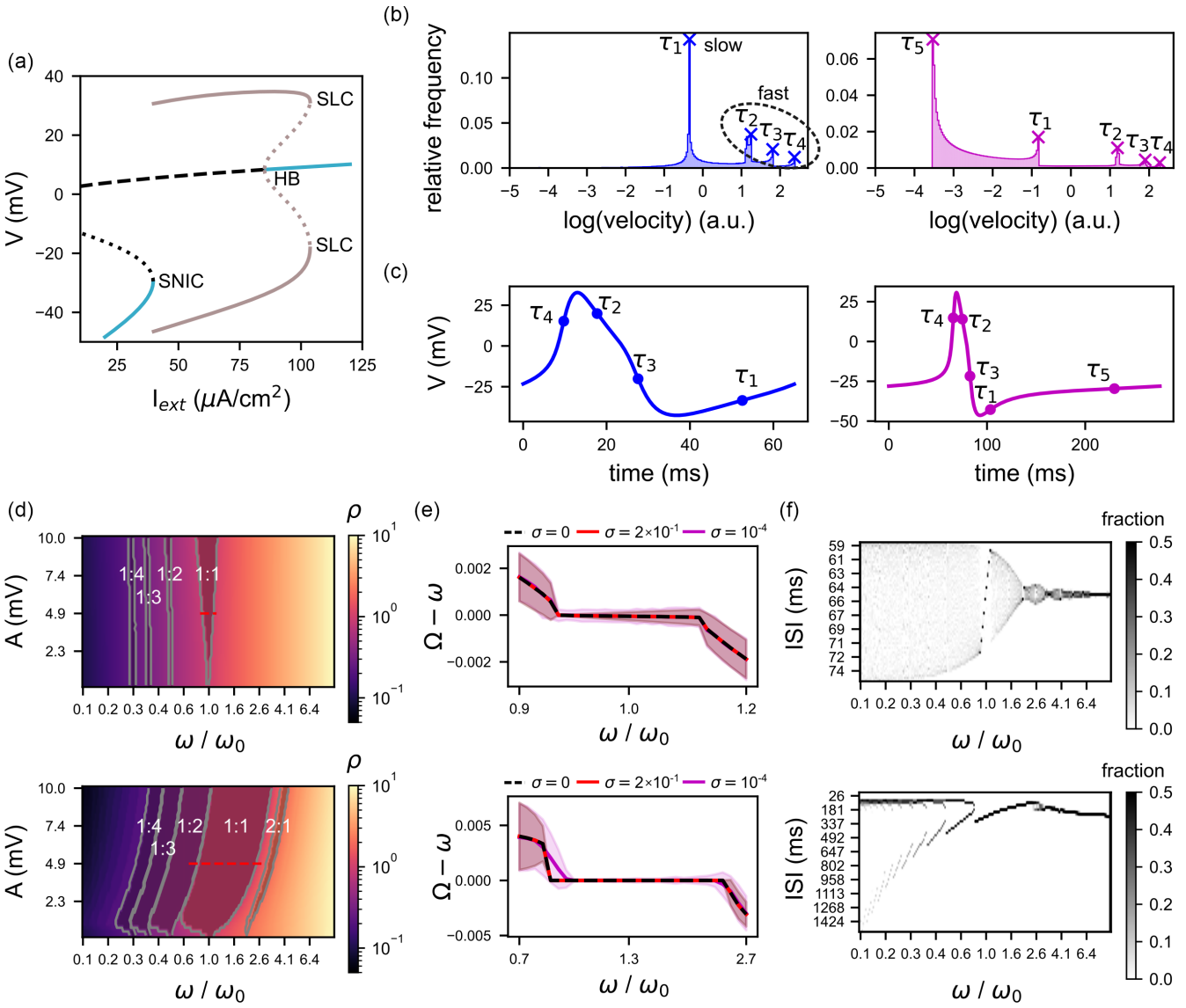


FIG. 6. Slow-fast and ghost-cycle regimes in the Morris-Lecar (ML) model. (a) Bifurcation diagram. Dashed black/gray line: unstable focus/limit cycle; gray line: stable limit cycle; dotted black line: saddle; teal line: stable fixed point. SNIC bifurcation at $I_{\text{ext}} = 39.69345$ μA/cm^2. (b) Histograms of the velocity distributions from the system's trajectories in the slow-fast regime (left) at $I_{\text{ext}} = 55$ μA/cm^2 and the one-ghost cycle regime (right) at $I_{\text{ext}} = 40.19345$ μA/cm^2. Indicated peaks are taken as representative timescales of the systems. (c) Time series of a single period of the ML system in the slow-fast regime (left) and one-ghost cycle regime (right). (d)–(f) Response of the ML system in the slow-fast (top row) and one-ghost cycle regime (bottom row) to periodic forcing. (d) Corresponding Arnold tongues indicate areas of n:m entrainment as a function of the amplitude A and frequency ω of the forcing (normalized to ω_0). Color encodes the winding number $\rho = \frac{T_{\text{out}}}{T_{\text{in}}}$. (e) Difference of the observed frequency Ω and the forcing frequency ω at various noise intensities in the parameter range indicated by the dashed red lines in (d). Plateaus correspond to cross sections through the 1:1 entrainment tongues. (f) Distribution of the interspike intervals (ISIs) as a function of the forcing frequency. Parameters for (a)–(f): $C_m = 20$ (μF/cm^2), $V_1 = -1.2$ (mV), $V_2 = 18$ (mV), $V_3 = 12$ (mV), $V_4 = 17$ (mV), $g_L = 2$ (mS/cm^2), $g_K = 8$ (mS/cm^2), $g_{Ca} = 4$ (mS/cm^2), $\phi = 0.06667$ (s^{-1}), $V_L = -60$ (mV), $V_K = -80$ (mV), $V_{Ca} = 120$ (mV).

display type-I neuronal activity (cf. [43,44] for biophysical details). In type-I neurons, oscillations are initiated via a single SNIC bifurcation as a function of an external input current I_{ext} [Fig. 6(a)], thus allowing the emergence of a one-ghost cycle when organized close to the SNIC. In this study, we chose $I_{\text{ext}} = 55$ μA/cm^2 for the slow-fast regime and $I_{\text{ext}} = 40.19345$ μA/cm^2 for the one-ghost cycle regime. Other parameters are as specified in Fig. 6.

Numerical analysis of the timescales of the systems shows that the type-I ML neurons feature several characteristic timescales corresponding to the complex shape of the relaxation oscillations [Figs. 6(b) and 6(c), left]. For simplicity, we consider $\tau_2 - \tau_4$ to constitute the fast timescale, since they define the shape of a single spike. Similar to the VdP_{1g} system, however, the additional slow timescale of the one-ghost cycle that emerges close to the SNIC bifurcation dominates the dynamics of the ML oscillator [Figs. 6(b) and 6(c), right]. In the periodically forced ML oscillator and its one-ghost variant, we find equivalent entrainment capabilities with robustness to noise, bursting behavior, and changes in the ISI distributions

as described for the VdP and VdP_{1g} models [Figs. 6(d)–6(f) and Supplemental Material Fig. 5].

2. *Slow-fast and two-ghost cycle dynamics in an ecological model*

To study the dynamics of another two-ghost cycle model, we consider a model of a simple freshwater ecosystem described by van Nes and colleagues [45]. Shallow lakes have been observed to exhibit cyclical shifts between a clear water state and a turbid state [45–47]. In the turbid states, the lakes are devoid of submerged macrophytes, and excessive nutrient loading has caused most lakes in populated areas to shift to such a state. Upon reduction of the nutrient loading, the lakes can shift back to the clear state, but the critical nutrient level at which the shift back occurs is typically lower than the nutrient level at which the ecosystem switched to the turbid state in a hysteresis-like behavior. In some ecosystems, regular oscillations in total phosphorus in the water column (P_w) and vegetation cover (V) with a period of approximately 7 years have been observed [48,49]. In [45], two mechanisms of how such cycles may emerge have been proposed. In particular, the following model describes the dynamics of vegetation and phosphorus in the lake's water:

$$\begin{aligned}
\frac{dV}{dt} &= r_V V\left(1-\frac{V\left(h_E^{p_e}+E^{p_e}\right)}{h_E^{p_e}}\right)\\
\frac{dP_w}{dt} &= \frac{P_{w,\mathrm{in}}-P_w}{\tau}+g\frac{\mathrm{SOD}^{p_{\mathrm{SOD}}}}{\mathrm{SOD}^{p_{\mathrm{SOD}}}+H_{\mathrm{SOD}}^{p_{\mathrm{SOD}}}}+\frac{A\sin(\omega t)}{\tau}\\
\mathrm{SOD} &= \frac{k_V V}{l_{\mathrm{SOD}}},\quad E=\gamma_E P_w\frac{h_V}{h_V+V}.
\end{aligned} \tag{6}$$

There are two basic assumptions in this model: First, the growth of vegetation is limited by the turbidity of the water E, which grows with increasing phosphorus concentration P_w, but is also diminished by increasing vegetation V. Second, based on observations [50], it is assumed that vegetation can lead to an increase in sediment oxygen demand (SOD) due to an increased amount of organic material (pieces of dead vegetation) that is buried in the sediment and degraded by bacteria consuming oxygen. However, this dynamical process is given as a quasi-steady-state expression because of the much faster timescale of this degradation process, leading to an enhanced release of phosphorus under anoxic conditions. Both processes constitute feedback mechanisms taken into account in the model and lead to oscillations of phosphorus in the water and vegetation. Here, r_V is the maximum growth rate of vegetation, h_E is a threshold of light attenuation, p_e is the dimensionless exponent in the Hill function of the positive vegetation effect, τ is the retention time, $P_{w,\mathrm{in}}$ is the phosphorus concentration of incoming water normalized to mean depth, g represents the maximum sediment phosphorus release rate, p_{SOD} determines the steepness of the increase of sediment phosphorus release around the critical value H_{SOD}, k_V describes the buildup of SOD due to vegetation, and l_{SOD} the first-order decay of SOD. E represents turbidity as vertical light attenuation (m^{-1}), γ_E is the relation between total phosphorus and light attenuation, and h_V is the vegetation cover with half of the maximal effect on water clarity. We modified the model by adding the forcing term $A\sin(\omega t)$ to the total phosphorus equation that we scaled by the retention time, and that may reflect periodic external influxes e.g., due to seasonal or other processes. For this study, the exact origin of the forcing, however, does not matter. The parameter values used here are given in Fig. 7.

In our study, we use a decreased sediment phosphorus release rate g, a slightly lower critical sediment oxygen demand H_{SOD}, and a slightly higher phosphorus influx $P_{w,\mathrm{in}}$ compared to the values used by van Nes and colleagues who used $g = 2\times10^{-3}\,(\mathrm{gm^{-3}d^{-1}})$, $H_{\mathrm{SOD}} = 2\,(\mathrm{gm^{-2}})$, $P_{w,\mathrm{in}} = 0.05\,(\mathrm{gm^{-2}})$ [45]. For increasing values of p_e, oscillations are then initiated by a Hopf-bifurcation at $p_e \approx 2.52$ and by two SNIC bifurcations at $p_e \approx 4.02$ and $p_e \approx 4.03$, respectively [Fig. 7(a)]. Close to these SNIC bifurcations, a two-ghost cycle emerges. We consider the value $p_e = 2.85$ for conventional slow-fast dynamics and $p_e = 4.014$ for a two-ghost cycle. As expected, long transients due to the ghosts emerge in the time series [Figs. 7(b) and 7(c)]. Due to slightly different positions of the two SNIC bifurcations on the p_e axis, these are numerically characterized as distinct slow timescales [Fig. 7(b)]. In the context of periodic forcing, however, these differences seem irrelevant as the entrainment properties [Fig. 7(d)], robustness to noise [Fig. 7(e)], and ISI-spike distributions [Fig. 7(f)] are qualitatively very similar to the VdP_{2g} system. The only qualitative difference we note here is the absence of chaos in the van Nes two-ghost cycle model in the regime considered here. Note for Fig. 7(e), in contrast to the other systems considered in this manuscript, we used multiplicative noise instead of additive noise to avoid negative values that would not be meaningful for the variables of this model (vegetation coverage and phosphorus concentration). We thus modified the above approach by multiplying the noise term with the respective variables $\dot{X}(t) = f(X(t),t)dt + X(t)dW(t)$.

III. DISCUSSION AND CONCLUSION

Oscillatory processes with multiple timescales are common in nature and are often described as slow-fast systems. These systems have a small parameter ε that creates a separation between slow and fast dynamics. Using classical perturbation methods, many properties of the dynamics of slow-fast systems, such as the VdP oscillator, are well understood by considering the dynamics on the critical manifold. By contrast, the dynamics of ghost cycles such as the modified VdP_{2g} system are dominated by trapping, giving rise to the slow timescale, and sequential rapid transitions between ghost states. Contrary to the critical and slow manifolds of slow-fast systems, these ghost states are weakly attracting, noninvariant [33], and nonhyperbolic [31]. As we have shown here, the different origins of the slow dynamics lead to unique responses under periodic forcing: the dynamics of the forced VdP system remain close to the unforced system with limited entrainment (for low forcing amplitudes); ghost cycles, however, show a surprising ability to be entrained by the periodic forcing signal, reflected by the size of the Arnold tongues, but also exhibit qualitatively new responses (e.g., bursting).

These differences in the responses of slow-fast oscillators and ghost cycles can be understood from the nonautonomous description of these systems. In the case of the classical VdP system, external forcing does not affect the qualitative organization of the phase space. An important characteristic

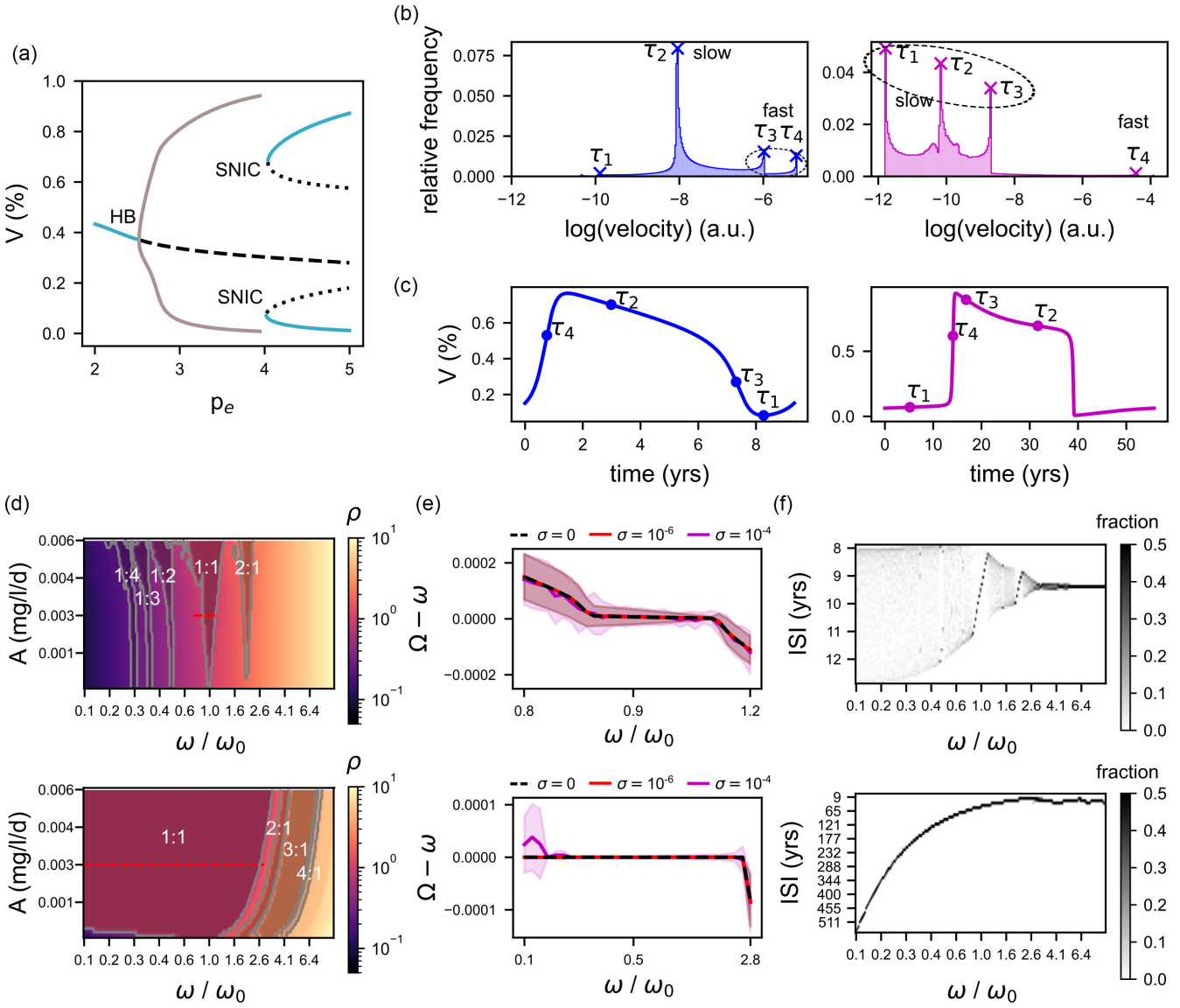


FIG. 7. Slow-fast and ghost-cycle regimes in the van Nes model. (a) Bifurcation diagram. Dashed black line: unstable focus; gray line: stable limit cycle; dotted black line: saddle; teal line: stable fixed point. SNIC bifurcations at $p_e = 4.02$. (b) Histograms of the velocity distributions from the system's trajectories in the slow-fast regime (left) at $p_e = 2.85$ and the one-ghost cycle regime (right) at $p_e = 4.014$. Indicated peaks are taken as representative timescales of the systems. (c) Time series of a single period of the van Nes system in the slow-fast regime (left) and two-ghost cycle regime (right). (d)–(f) Response of the van Nes system in the slow-fast (top row) and two-ghost cycle regime (bottom row) to periodic forcing. (d) Corresponding Arnold tongues indicate areas of n:m entrainment as a function of the amplitude A and frequency ω of the forcing (normalized to ω_0). Color encodes the winding number $\rho = \frac{T_{\text{out}}}{T_{\text{in}}}$. (e) Difference of the observed frequency Ω and the forcing frequency ω at various noise intensities in the parameter range indicated by the dashed red lines in (d). Plateaus correspond to cross sections through the 1:1 entrainment tongues. (f) Distribution of the interspike intervals (ISIs) as a function of the forcing frequency. Parameters used in (a)–(f): $r_V = 0.07$ (d^{-1}), $h_E = 1$ (m^{-1}), $\gamma_E = 30$ (m^2g^{-1}), $P_{w,\text{in}} = 0.08565$ (gm^{-2}), $\tau = 475$ (d), $g = 7.59 \times 10^{-5}$($\text{gm}^{-3}\text{d}^{-1}$), $p_{\text{SOD}} = 10$, $H_{\text{SOD}} = 1.52$ (gm^{-2}), $l_{\text{SOD}} = 0.01$ (d), $\text{h}_\text{V} = 0.2$, $\text{k}_\text{V} = 0.05$ (gm^{-2}d).

of ghost cycles, however, is that they generally emerge at criticality in the sense of closeness to one or more SNIC bifurcations. This enables even small amplitude forcing to create and destroy fixed points and ghost attractors, resulting in a continuous remodeling of the system's attractor landscape in response to the time-varying input defined by the periodic forcing. It is exactly this landscape changing over time that determines how the system's trajectory evolves. The response behavior, therefore, depends on the number of ghosts, their particular arrangement and organization in phase space in the nonautonomous system, and on the frequency of the forcing that leads to the attractor landscape changes. In particular, the nonautonomous system analysis undertaken here highlights that systems can have very different mechanisms that lead to entrainment, depending on how exactly the topology of the phase space changes with the external forcing, but also on how fast these changes take place. To our knowledge, this is the first time that entrainment of a system has been described as a

rate-dependent boundary-crossing process [40], which could stimulate further research in this direction. Importantly, the features of ghost cycles described here are generic and can readily be reproduced in one-ghost and two-ghost cycles from other models.

Ghost cycles appear to be typical for large classes of models. Recently proposed gene-regulatory network models are characterized by three simultaneous SNIC bifurcations [51–53] giving rise to three-ghost cycles [31], and models of recurrent neuronal networks [54] suggest the existence of cycles between four or more ghosts. Since the response of ghost cycles to periodic forcing depends on the orientation of the phase flow that is organized by the ghosts, it will be interesting to study the response properties of multi-ghost cycles to periodic or more complex forcing. Given that many of the one- and multi-ghost cycles seem to be typical for biological models, we speculate that the flexibility (being able to exploit different dynamics via the changes in the attractor landscape) and robustness in the response to external forcing that emerges in these models could be a feature that biological networks evolved to exploit for information processing or biological computation. In agreement with this hypothesis, Choi *et al*. recently showed that a one-ghost cycle in the dynamics of *Drosophila* olfactory receptor neurons enhances temporal information encoding, allowing efficient transfer of information about the timing, duration, and intensity of odor fluctuations [55]. As ghost cycles emerge when a system is organized at criticality, i.e., close to one or more SNIC bifurcations, biological systems may exhibit feedback mechanisms for self-organization close to the critical point that enable them to utilize the computational capabilities of ghost cycles [38,56,57]. Future studies are thus required to test these hypotheses in the context of models for computational tasks in biological networks.

ACKNOWLEDGMENTS

D.K. received funding by an EMBO Fellowship (Grant No. ALTF 310-2021), A.K. acknowledges funding by the Lise Meitner Excellence Programme of the Max Planck Society, and U.F. acknowledges support by the Deutsche Forschungsgemeinschaft (German Science Foundation) (Grant No. 454054251).

DATA AVAILABILITY

The data that support the findings of this article are openly available [58].

[1] T. Roenneberg and M. Merrow, Curr. Biol. **26**, R432 (2016).
[2] G. Brabant, K. Prank, and C. Schofl, Trends Endocrinol. Metab. **3**, 183 (1992).
[3] L. Glass, Nature (London) **410**, 277 (2001).
[4] E. Izhikevich, *Dynamical Systems in Neuroscience: The Geometry of Excitability and Bursting* (The MIT Press, 2006).
[5] R. Noyes and R. Field, Annu. Rev. Phys. Chem. **25**, 95 (1974).
[6] A. Goldbeter, FEBS Lett. **587**, 2778 (2013).
[7] V. Volterra, Nature (London) **118**, 558 (1926).
[8] C. Elton and M. Nicholson, J. Anim. Ecol. **11**, 215 (1942).
[9] B. Blasius, L. Rudolf, G. Weithoff, U. Gaedke, and G. Fussmann, Nature (London) **577**, 226 (2020).
[10] A. Liebhold, W. Koenig, and O. Bjørnstad, Annu. Rev. Ecol. Evol. Syst. **35**, 467 (2004).
[11] C. Wang, C. Deser, J.-Y. Yu, P. DiNezio, and A. Clement, El niño and southern oscillation (ENSO): A review, in *Coral Reefs of the Eastern Pacific*, edited by P. Glymn, D. Manzello, and I. Enochs (Springer Science Publisher, 2016), pp. 85–106.
[12] H. Dijkstra and M. Ghil, Rev. Geophys. **43**, 2002RG000122 (2005).
[13] G. Vettoretti and W. Peltier, J. Clim. **31**, 3423 (2018).
[14] N. G. I. C. P. members, Nature (London) **431**, 147 (2004).
[15] J.-M. Liu, Laser oscillation, *Principles of Photonics* (Cambridge University Press, 2016), pp. 274–296.
[16] C. Kuehn, *Multiple Time Scale Dynamics* (Springer International Publishing, 2015).
[17] R. Bertram and J. Rubin, Math. Biosci. **287**, 105 (2017).
[18] N. Fenichel, Indiana Univ. Math. J. **21**, 193 (1971).
[19] N. Fenichel, J. Diff. Equ. **31**, 53 (1979).
[20] K. Rossi, R. Budzinski, E. Medeiros, B. Boaretto, L. Muller, and U. Feudel, Phys. Rev. E **111**, 021001 (2025).
[21] P. beim Graben, A. Jimenez-Marin, I. Diez, J. Cortes, M. Desroches, and S. Rodrigues, Front. Comput. Neurosci. **13**, 62 (2019).
[22] S. Kato, H. Kaplan, T. Schrödel, S. Skora, T. Lindsay, E. Yemini, S. Lockery, and M. Zimmer, Cell **163**, 656 (2015).
[23] T. Woo, X. Liang, D. Evans, O. Fernandez, F. Kretschmer, S. Reiter, and G. Laurent, Nature (London) **619**, 122 (2023).
[24] P. Sanchez, V. Mochulska, C. Denis, G. Mönke, T. Tomita, N. Tsuchida-Straeten, Y. Petersen, K. Sonnen, P. François, and A. Aulehla, eLife **11**, e79575 (2022).
[25] M. Meeuse, Y. Hauser, L. Moya, G.-J. Hendriks, J. Eglinger, G. Bogaarts, C. Tsiairis, and H. Großhans, Mol. Syst. Biol. **16**, e9498 (2020).
[26] C. Bieg, H. Vallès, A. Tewfik, B. Lapointe, and K. McCann, Ecosystems **27**, 310 (2024).
[27] A. Hastings, K. Abbott, K. Cuddington, T. Francis, G. Gellner, Y. Lai, A. Morozov, S. Petrovskii, K. Scranton, and M. Zeeman, Science **361**, eaat6412 (2018).
[28] M. Rabinovich, A. Volkovskii, P. Lecanda, R. Huerta, H. D. I. Abarbanel, and G. Laurent, Phys. Rev. Lett. **87**, 068102 (2001).
[29] V. Afraimovich, V. Zhigulin, and M. Rabinovich, Chaos **14**, 1123 (2004).
[30] P. Ashwin and C. Postlethwaite, Physica D **265**, 26 (2013).
[31] D. Koch, A. Nandan, G. Ramesan, I. Tyukin, A. Gorban, and A. Koseska, Phys. Rev. Lett. **133**, 047202 (2024).
[32] A. Gorban, Electron. J. Differ. Equ. **1**, 05 (2004).
[33] A. Gorban, I. Tyukin, E. Steur, and H. Nijmeijer, SIAM J. Control Optim. **51**, 2306 (2013).

[34] B. van der Pol and J. van der Mark, Lond. Edinb. Dubl. Phil. Mag. J. Sci. **6**, 763 (1928).
[35] See Supplemental Material at http://link.aps.org/supplemental/10.1103/3d9z-qrb1 for details on methods and Supplemental figures.
[36] A. Pikovsky, M. Rosenblum, and J. Kurths, *Synchronization: A Universal Concept in Nonlinear Sciences* (Cambridge University Press, 2001).
[37] B. Verd, A. Crombach, and J. Jaeger, BMC Syst. Biol. **8**, 43 (2014).
[38] A. Stanoev, A. Nandan, and A. Koseska, Mol. Syst. Biol. **16**, e8870 (2020).
[39] U. Feudel, Nonlinear Processes Geophys. **30**, 481 (2023).
[40] A. Basak, K. Dana, N. Bairagi, and U. Feudel, Chaos **34**, 093105 (2024).
[41] P. Ashwin, S. Wieczorek, R. Vitolo, and P. Cox, Philos. Trans. R. Soc. A **370**, 1166 (2012).
[42] P. D. L. Ritchie, H. Alkhayuon, P. M. Cox, and S. Wieczorek, Earth Syst. Dyn. **14**, 669 (2023).
[43] C. Morris and H. Lecar, Biophys. J. **35**, 193 (1981).
[44] K. Tsumoto, H. Kitajima, T. Yoshinaga, K. Aihara, and H. Kawakami, Neurocomputing **69**, 293 (2006).
[45] E. van Nes, W. Rip, and M. Scheffer, Ecosystems **10**, 17 (2007).
[46] J. Shapiro and D. Wright, Freshwater Biol. **14**, 371 (1984).
[47] M. Scheffer, *Ecology of Shallow Lakes* (Chapman and Hall, London, 1998).
[48] M. Perrow, B. Moss, and J. Stansfield, Hydrobiologia **275-276**, 43 (1994).
[49] W. Rip, M. Ouboter, E. van Nes, and B. Beltman, Arch. Hydrobiol. **164**, 387 (2005).
[50] L. Lijklema, in *Interactions Between Sediments and Freshwater*, edited by H. L. Golterman (W. Junk Publishers, The Hague, 1977), pp. 313–317.
[51] L. Jutras-Dubé, E. El-Sherif, and P. François, eLife **9**, e55778 (2020).
[52] S. Farjami, K. Sosa, J. Dawes, R. Kelsh, and A. Rocco, J. R. Soc. Interface **18**, 20210442 (2021).
[53] L. Yang, A. Jia, W. Sun, and M. Turcotte, Nonlinear Dyn. **109**, 1081 (2022).
[54] I. Jordan, P. Sokół, and I. Park, Front. Comput. Neurosci. **15**, 678158 (2021).
[55] K. Choi, W. Rosenbluth, I. R. Graf, N. Kadakia, and T. Emonet, PRX Life **2**, 043011 (2024).
[56] D. Durstewitz, J. Neurosci. **23**, 5342 (2003).
[57] I. Graf and B. Machta, Proc. Natl. Acad. Sci. USA **121**, e2308215121 (2024).
[58] https://github.com/KochLabCode/2025_GhostCycles.